Supplementary Materials for
A 26-Gram Butterfly-Inspired Robot Achieving Autonomous Tailless Flight

Weibin Gu *et al.*
Corresponding authors: Weibin Gu, Chao Gao, Guyue Zhou
Email: chao.gao@cantab.net, {guweibin, zhouguyue}@air.tsinghua.edu.cn

This PDF file includes:

Materials and Methods
Supplementary Text
Figures S1 to S5
Tables S1 to S2
Captions for Movies S1 to S5

Other Supplementary Materials for this manuscript:

Movies S1 to S5

Materials and Methods

Fabrication of robot components

The fuselage and wing-servo connectors were 3D printed in polyethylene terephthalate glycol (PETG) using fused-deposition modeling. PETG was selected over polylactic acid (PLA) and thermoplastic polyurethane (TPU) for its combination of rigidity and impact resistance, allowing the structure to endure cyclic inertial loads during sustained flapping.

Wings were fabricated from Mylar film reinforced with carbon fiber spars (a 1.0 mm main spar, 0.8 mm leading edge and hindwing contour, and 0.5 mm longitudinal veins). The carbon reinforcement provided a high stiffness-to-weight ratio and enabled spatial stiffness gradients analogous to those found in butterfly wings. Alternative membranes were evaluated: TPU exhibited excessive compliance and poor adhesion, while silicone-coated polyamide (PA66) offered durability but imposed excessive mass. All tested membranes were flight-capable; however, PET was ultimately chosen for its balance of light weight, stiffness, tear resistance, adhesive compatibility, and optical transparency for motion capture. Wing fabrication involved laser-printing a venation template, overlaying the PET film, and bonding carbon rods using UV-curable adhesive and cyanoacrylate. Left-right wing pairs were mass-balanced within 0.05 g ($\leq 1\%$ of a single wing mass) to minimize asymmetries that could induce unbalanced aerodynamic forces or fuselage vibrations from uneven stroke timing or deformation [32].

Commercial micro servos (BlueArrow D30T MG HV, 4.6 g each) were selected for their high torque-to-weight ratio and metal geartrain, minimizing backlash under dynamic loading. Metal servo arms were used to prevent torsional deformation observed with plastic arms, which degraded stroke symmetry and amplitude. Although lighter custom actuators with planetary gearboxes could further reduce mass, off-the-shelf servos were preferred for their reliability, reproducibility, and ease of integration.

The onboard embedded system is based on an ESP32-S3-WROOM-1-N16R8 (dual-core 32-bit Xtensa LX7, 240 MHz, 16 MB Flash, 8 MB PSRAM), supporting parallel real-time wing actuation and wireless communication with a custom ground control station for data logging and monitoring. Power is supplied by 1S or 2S LiPo batteries through a multi-stage regulation system: a buck converter provides 3.3 V to the controller and sensors, a boost circuit delivers 8.2 V to the servos for consistent torque under high load, and an LDO outputs 5 V to the ExpressLRS module. The ELRS module serves only as a safety override for manual control. Servo current and power consumption are monitored via INA219 sensors. The sensor suite includes an ICM-42688-P IMU (±16 g, ±2000 °/s, 32 kHz), BMM350 magnetometer ($\pm 2000\,\mu$T, 400 Hz), and BMP390L barometer (±3 Pa, 200 Hz) for real-time state estimation.

Forewing contour parameterization

Sampled wing contour (data points $\{\mathbf{D}_j\}_{j=1}^{N}$) were represented by a periodic cubic B-spline. The spline curve is defined as

$$\mathbf{C}(u) = \sum_{i=0}^{n-1} N_{i,3}(u)\,\mathbf{P}_i, \qquad u \in [0,1], \tag{S1}$$

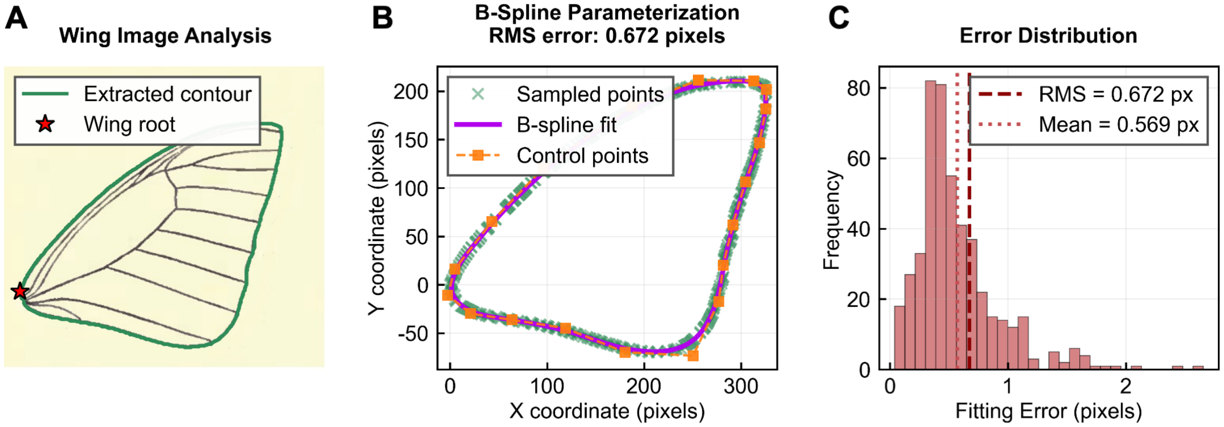

Figure S1: **Forewing contour parameterization.**

where $\{\mathbf{P}_i\}_{i=0}^{n-1}$ are the spline control points determined by smoothing least-squares fitting, and $N_{i,3}(u)$ are the cubic B-spline basis functions defined by the Cox-deBoor recursion [78] as

$$N_{i,0}(u) = \begin{cases} 1, & u_i \leq u < u_{i+1}, \\ 0, & \text{otherwise}, \end{cases} \tag{S2}$$

$$N_{i,p}(u) = \frac{u - u_i}{u_{i+p} - u_i} N_{i,p-1}(u) + \frac{u_{i+p+1} - u}{u_{i+p+1} - u_{i+1}} N_{i+1,p-1}(u), \tag{S3}$$

with the convention that any fraction with a zero denominator is taken as zero. A periodic knot vector $\mathbf{U}$ was used to ensure closure and C^2 continuity.

Raw contours were cyclically reordered to start at the wing root and closed by appending the start point (fig. S1A). Parameter values were assigned by chord length as

$$t_k = \frac{\sum_{m=1}^{k-1} \|\mathbf{D}_{m+1} - \mathbf{D}_m\|}{\sum_{m=1}^{N} \|\mathbf{D}_{m+1} - \mathbf{D}_m\|}, \quad t_1 = 0,\ t_{N+1} = 1, \tag{S4}$$

and a periodic smoothing cubic spline was fitted to $(t_k, \mathbf{D}_k)$ by least-squares with smoothing factor $s = \alpha N$ ($\alpha = 0.5$ herein). The fitted spline was resampled at $M = 1000$ uniformly spaced $u \in [0, 1]$ to yield a dense curve $\widetilde{\mathbf{C}}$. Fit quality was quantified by nearest-neighbor errors as

$$e_j = \min_{q \in \widetilde{\mathbf{C}}} \|\mathbf{D}_j - q\|, \qquad \text{RMS} = \sqrt{\frac{1}{N} \sum_{j=1}^{N} e_j^2}. \tag{S5}$$

The parameterization results from the above analysis were reported in Table S1 and the control points $\mathbf{P}_i = (x_i, y_i)$ for the forewing spline representation were summarized in Table S2. The fitting procedure achieved an RMS error of 0.672 pixels (fig. S1B), corresponding to a relative error of 0.13% of the wing span. The error distribution (fig. S1C) shows that 95% of contour points were fitted with errors less than 1.5 pixels, demonstrating the high accuracy of the B-spline representation while maintaining C^2 continuity. This parameterization procedure produced smooth, reproducible wing contours suitable for CAD modeling

Table S1: **Parameterization settings and results for forewing contour.**

Parameter	**Value**	**Units**
Sampled points (N)	477	points
Control points (n)	22	points
Data reduction	95.4%	–
RMS fitting error	0.672	pixels
Smoothing factor (α)	0.5	–
Resampled points (M)	1000	points

Table S2: **Control points for periodic cubic B-spline representation of forewing contour.**

Index i	x_i (pixels)	y_i (pixels)	Index i	x_i (pixels)	y_i (pixels)
0	312.908971	-210.627073	11	176.467499	51.938866
1	256.030813	-211.484444	12	220.083362	52.401279
2	187.390279	-184.698024	13	263.699226	52.863692
3	95.897335	-120.190052	14	307.315090	53.326105
4	43.167102	-65.320731	15	338.611816	41.334592
5	4.851825	-16.166765	16	349.589403	11.000153
6	-2.349460	10.755896	17	340.247852	-29.334286
7	21.089190	29.768771	18	310.587162	-69.668725
8	63.968615	36.324384	19	260.607334	-110.003164
9	118.976443	44.915320	20	190.308367	-150.337603
10	147.655635	48.477453	21	99.690262	-190.672042

and aeroelastic analysis, with the compact control point representation enabling efficient computational modeling while preserving biological accuracy.

Biological wing venation analysis

Forewing images were collected primarily from published literature with documented clear venation patterns [79], supplemented by photographs of museum-grade specimens available from open-access sources (Wikipedia). Specimens were selected based on strict visibility criteria requiring a fully unobstructed forewing (dorsal or ventral) view with distinct Dc and Cu1 veins, which define key geometric axes for comparative analysis. The dense and pigmented scales on butterfly wings often obscure vein boundaries, substantially constraining the number of usable samples. Consequently, the final dataset included 24 different specimens representing three families, namely Nymphalidae ($n = 8$), Pieridae ($n = 8$), and Papilionidae ($n = 8$). For each specimen, the forewing image was first converted to grayscale and manually annotated with yellow solid lines indicating the Dc and Cu1 veins (fig. S2). The annotated regions were then segmented in HSV color space to extract the obtuse inter-vein Dc-Cu1 angle. Future morphological studies could expand statistical results by employing chemical bleaching or depigmentation techniques to enhance venation contrast and enable automated image segmentation.

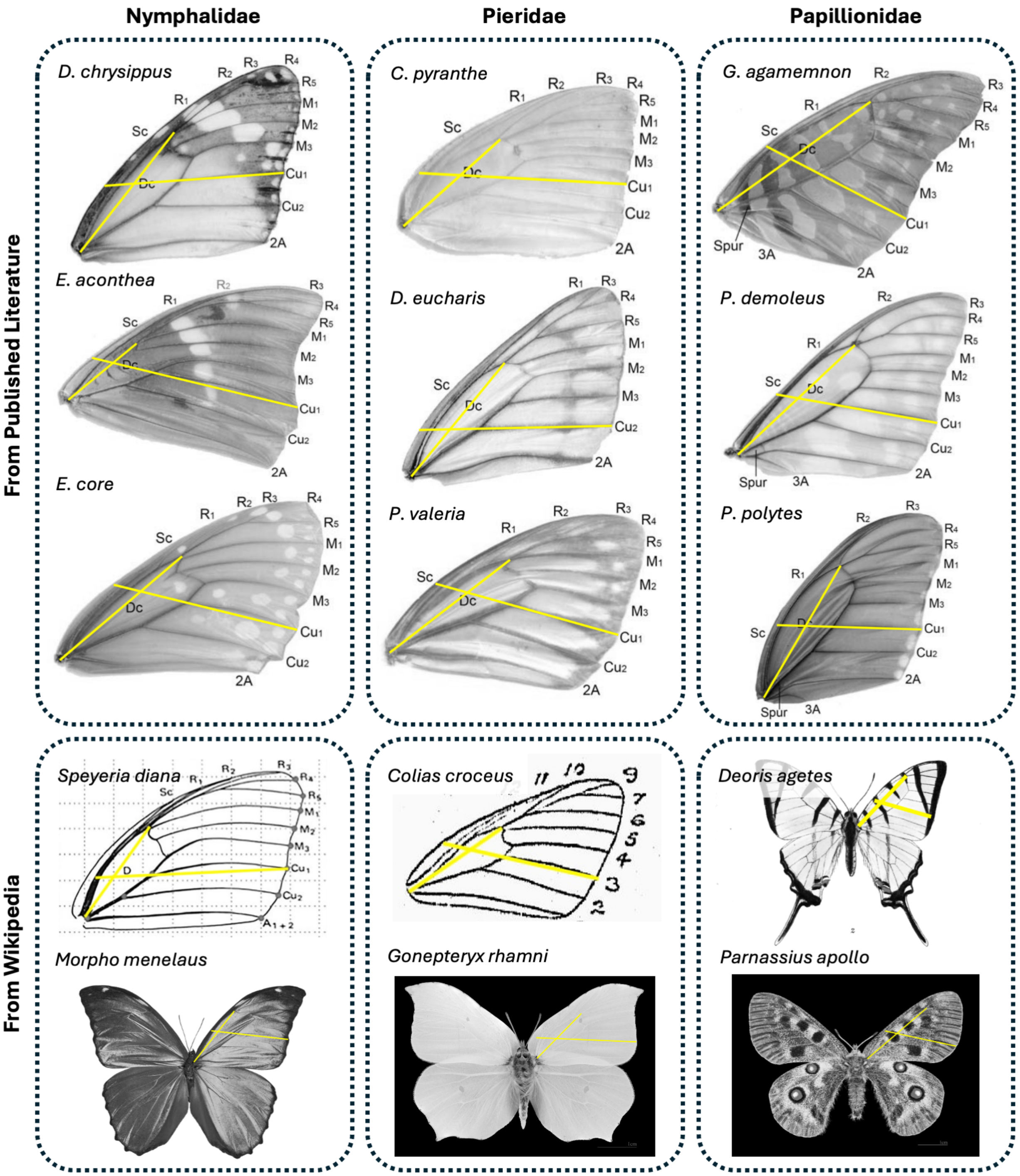

Figure S2: **Quantification of forewing Dc-Cu1 venation angle across butterfly families.**

Wing performance analysis

Wing performance was assessed using a custom flapping apparatus (Fig. 2D). Retroreflective stickers were selected for their low mass, which is the lightest available option despite still adding some weight. Increasing the number or size of markers could improve tracking accuracy but would also alter wing dynamics due to extra weight.

Each wing variant underwent same flapping cycles while synchronized force and kinematic data were recorded at 222 Hz. The raw force signals were processed through a computational pipeline that first identified active flapping periods by detecting servo motor activation thresholds in the PWM command signals. Stroke reversal points were determined via second-order differentiation of positional data to precisely segment individual flapping cycles. Aerodynamic forces were isolated by subtracting inertial contributions using a phase-locked averaging approach. Specifically, a perforated counterpart was fabricated for each wing variant to approximate the original mass and inertial properties while substantially reducing aerodynamic loading. Forces measured under identical flapping conditions with these perforated wings were treated as inertial baselines and subtracted from the corresponding intact-wing measurements. For each wing configuration, 40 consecutive flapping cycles were selected from steady-state operation and processed with a fourth-order Butterworth low-pass filter (50 Hz cutoff) to remove high-frequency noise. The filtered force data were temporally normalized to the interval $[0, 1]$ to enable cycle-wise comparison. Component-wise force signals (F_x, F_y, F_z) were then averaged and their variances computed to characterize aerodynamic force profiles across the normalized flapping period. Processed forces were further analyzed via polar coordinate transformation, where the angular coordinate represented normalized time ($\theta_{\text{polar}} = 2\pi t_{\text{norm}}$) and the radial coordinate denoted force magnitude with an offset ensuring positivity (Fig. 2, F and G). Time-integrated forces were computed using trapezoidal numerical integration for both signed and absolute components, providing quantitative measures of net impulse and cumulative force production. This analysis enabled comprehensive comparison of force magnitude, temporal phasing, and generation patterns across different wing morphological variants.

Wing deformation was quantified by projecting three-dimensional marker positions onto a plane orthogonal to the wing rotation axis, isolating bending motion from the overall flapping trajectory. Bending angles were defined as the angular deviation between proximal and distal segments, with maxima identified separately for downstroke and upstroke phases (Fig. 2, I and J). Hindwing kinematics were characterized by computing elevation angles relative to the wing hinge throughout each flapping cycle. Forewing kinematics were derived from markers placed along the anterior (leading edge) and posterior (trailing edge) margins of each wing section, enabling direct quantification of instantaneous wing orientation relative to the airflow. Discrete marker data were interpolated to generate continuous angle-time curves, enabling phase-resolved comparison of fore-/hind-wing kinematics across wing variants.

Analytical properties of STAR

(i) Cycle-averaged frequency invariance. For constant A, the cycle-averaged flapping period is

$$T = \int_0^{2\pi} \frac{d\omega}{\dot{\omega}} = \frac{1}{\pi f} \int_0^{2\pi} p(\omega)\, d\omega = \frac{1}{f}, \tag{S6}$$

so STAR skews intra-cycle timing without altering the mean flapping frequency.

(ii) Linear stroke asymmetry. Choosing the phase origin such that the downstroke corresponds to $\omega \in [-\pi/2, \pi/2]$ and the upstroke to $\omega \in [\pi/2, 3\pi/2]$, the half-stroke durations are

$$T_{\text{down}} = \frac{1}{\pi f} \int_{-\pi/2}^{\pi/2} p(\omega)\, d\omega = \frac{1}{2f} + \frac{2A}{\pi f}, \tag{S7}$$

$$T_{\text{up}} = \frac{1}{2f} - \frac{2A}{\pi f}. \tag{S8}$$

Thus, the stroke asymmetry scales linearly with A, with the sign determining which half-stroke is prolonged, providing a monotonic tuning rule for control.

(iii) Smoothness and boundedness. Since $p(\omega)$ is smooth and strictly positive for $|A| < 0.5$, the reciprocal

$$r(\omega) = \frac{1}{p(\omega)}, \qquad \dot{\omega} = \pi f\, r(\omega), \tag{S9}$$

is bounded and continuous since

$$\frac{\pi f}{0.5 + |A|} \leq \dot{\omega} \leq \frac{\pi f}{0.5 - |A|}. \tag{S10}$$

As the stroke angle is a smooth function of $\sin(\omega)$, the resulting wing kinematics and its first derivative are also continuous.

Implementation of STAR

To avoid cumulative-phase drift induced by nonlinear inversion, the reciprocal variable $r = \frac{1}{p}$ is filtered using an IIR scheme. For a servo-based control loop with index n and update rate f_{servo}, the discrete implementation is

$$r_{\text{target}}[n] = \frac{1}{0.5 + A[n]\cos(\omega[n])}, \tag{S11}$$

$$r_{\text{smooth}}[n] = \alpha\, r_{\text{target}}[n] + (1 - \alpha)\, r_{\text{smooth}}[n-1], \tag{S12}$$

$$\Delta\omega[n] = \frac{\pi f}{f_{\text{servo}}}\, r_{\text{smooth}}[n], \tag{S13}$$

$$\omega[n+1] = \omega[n] + \Delta\omega[n], \tag{S14}$$

where $\alpha \in (0, 1)$ is the smoothing weight trading responsiveness for kinematic smoothness. The IIR filter cutoff f_c is tuned below the flapping frequency, leading to the intermediate choice

$$\alpha \approx \frac{2\pi f_c}{f_{\text{servo}}}, \tag{S15}$$

which is further refined based on experimental flight data to balance attitude response agility and wingstroke smoothness.

Online pitch estimation using recursive least squares

To stabilize pitch control in the presence of high-frequency body undulations, we implemented an online RLS estimator to extract the slowly varying mean of the measured pitch angle. Without loss of generality, the pitch signal can be modeled as

$$y(t) = a\sin(\omega t) + b\cos(\omega t) + c + \epsilon(t), \tag{S16}$$

where a and b describe the flapping-induced sinusoidal component at frequency ω, c is the low-frequency mean, and $\epsilon(t)$ represents measurement noise.

In discrete time with sampling index n and step Δt, the regression vector is

$$\boldsymbol{\varphi}_n = \begin{bmatrix} \sin(\omega t_n) \\ \cos(\omega t_n) \\ 1 \end{bmatrix}, \quad y_n = \boldsymbol{\varphi}_n^\top \boldsymbol{\theta} + \epsilon_n, \quad \boldsymbol{\theta} = [a, b, c]^\top, \tag{S17}$$

and the RLS updates follow

$$\boldsymbol{K}_n = \frac{\boldsymbol{P}_{n-1}\boldsymbol{\varphi}_n}{\lambda + \boldsymbol{\varphi}_n^\top \boldsymbol{P}_{n-1}\boldsymbol{\varphi}_n} \quad \text{(gain vector)}, \tag{S18}$$

$$e_n = y_n - \boldsymbol{\varphi}_n^\top \boldsymbol{\theta}_{n-1} \quad \text{(prediction error)}, \tag{S19}$$

$$\boldsymbol{\theta}_n = \boldsymbol{\theta}_{n-1} + \boldsymbol{K}_n e_n \quad \text{(parameter update)}, \tag{S20}$$

$$\boldsymbol{P}_n = \frac{1}{\lambda}\left[\boldsymbol{P}_{n-1} - \boldsymbol{K}_n \boldsymbol{\varphi}_n^\top \boldsymbol{P}_{n-1}\right] \quad \text{(covariance update)}, \tag{S21}$$

where $\lambda \in (0, 1]$ is the forgetting factor controlling adaptation speed. The low-frequency pitch signal for inner-loop control is obtained directly from the updated estimate c_n.

Futhermore, the regressor can be adapted using an instantaneous phase to account for variations in flapping frequency,

$$\varphi(t_n) = \int_0^{t_n} \omega_{\text{inst}}(\tau)\, d\tau, \tag{S22}$$

yielding

$$\boldsymbol{\varphi}_n^{\text{adaptive}} = \begin{bmatrix} \sin(\varphi(t_n)) \\ \cos(\varphi(t_n)) \\ 1 \end{bmatrix}. \tag{S23}$$

This frequency-aware regressor ensures robust tracking of the pitch mean under stroke timing modulation (with the instantaneous phase calculated from (2)).

Supplementary Text

Mathematical derivation and analysis of STAR

We analyzed two modulation function candidates for the stroke timing modulation parameter: (i) the sine variant $p = 0.5 + A(t)\sin(\omega)$, and (ii) the cosine variant $p = 0.5 + A(t)\cos(\omega)$. In the sequel, we show that only the cosine variant inherently eliminates persistent phase offsets correlated with initial conditions.

The wingstroke phase dynamics using the cosine variant are governed by

$$\frac{d\omega}{dt} = \frac{\pi f}{0.5 + A(t)\cos(\omega)}, \tag{S24}$$

$$\Rightarrow [0.5 + A(t)\cos(\omega)]\frac{d\omega}{dt} = \pi f, \tag{S25}$$

$$\Rightarrow \frac{d}{dt}[0.5\omega + A(t)\sin(\omega)] = \pi f + \dot{A}(t)\sin(\omega), \tag{S26}$$

$$\Rightarrow 0.5\omega(t) + A(t)\sin(\omega(t)) = \pi f t + \int_0^t \dot{A}(\tau)\sin(\omega(\tau))d\tau + C_0. \tag{S27}$$

Under antisymmetric modulation, $A_L(t) = -A_R(t) = A(t)$, subtracting the integrated equations for left and right wings yields

$$\begin{aligned} &0.5(\omega_L(t) - \omega_R(t)) + A_L(t)\sin(\omega_L(t)) - A_R(t)\sin(\omega_R(t)) = \\ &\qquad \int_0^t \dot{A}_L(\tau)\sin(\omega_L(\tau))\,d\tau - \int_0^t \dot{A}_R(\tau)\sin(\omega_R(\tau))\,d\tau + C_{L0} - C_{R0}. \end{aligned} \tag{S28}$$

Thus, the phase difference, defined as $\omega_L(t) - \omega_R(t)$, is

$$\Delta(t) = 2\left\{-A(t)\left[\sin(\omega_L(t)) + \sin(\omega_R(t))\right] + \int_0^t \dot{A}(\tau)\left[\sin(\omega_L(\tau)) + \sin(\omega_R(\tau))\right]d\tau + (C_{L0} - C_{R0})\right\}. \tag{S29}$$

For the sine variant $p = 0.5 + A(t)\sin(\omega)$, an analogous derivation gives

$$\Delta(t) = 2\left\{A(t)\left[\cos(\omega_L(t)) + \cos(\omega_R(t))\right] - \int_0^t \dot{A}(\tau)\left[\cos(\omega_L(\tau)) + \cos(\omega_R(\tau))\right]d\tau + (C_{L0} - C_{R0})\right\}. \tag{S30}$$

By comparing (S29) and (S30), it is straightforward to see that the steady-state phase difference Δ when $A(t) = 0$ arises from: (i) the constant initial condition offset $C_{L0} - C_{R0}$, and (ii) the history of modulation rate $\dot{A}$ coupled with wing phase terms.

The initial condition offset can be eliminated by using the cosine variant. Assuming symmetric initial conditions $\omega_L(0) = \omega_R(0) = 0$. Sine variant will have a persistent bias if $A(0) \neq 0$: $\Delta(0) = 2\left[A(0) + (C_{L0} - C_{R0})\right] = 0 \Rightarrow C_{L0} - C_{R0} = -2A(0)$. On the other hand, cosine variant demonstrates that the offset is independent of $A(0)$: $\Delta(0) = 2(C_{L0} - C_{R0}) = 0 \Rightarrow C_{L0} - C_{R0} = 0$. Thus, the cosine variant is preferred to avoid bias from initial conditions.

The integral term, which arises from the derivative expansion ($\dot{A}$), introduces phase drift during changes in A. To compensate, we can extend the phase dynamics (S24) as follows:

$$\frac{d\omega}{dt} = \frac{\pi f - \dot{A}(t)\sin(\omega)}{0.5 + A(t)\cos(\omega)}. \tag{S31}$$

This compensation is equivalent to subtracting the drift term $\int_0^t \dot{A}(\tau)\sin(\phi(\tau))d\tau$ from the output phase, ensuring continuity and eliminating phase drift during modulation transients. In particular, when A is constant or slowly time-varying, (S31) becomes the standard formulation (S24).

State estimation and PID tuning

Accurate and low-latency attitude estimation is critical for stable flight of the flapping-wing platform. We implemented a quaternion-based Madgwick filter [80] on the ESP32-S3 (dual-core 240 MHz with floating-point unit) to fuse IMU measurements in real time. This approach was selected for its low computational cost, fast convergence, and robustness under dynamic motion, outperforming complementary filters in accuracy and avoiding the high complexity and matrix operations of extended Kalman filters.

The Madgwick filter estimates orientation by minimizing accelerometer and magnetometer errors using a gradient descent approach. For 9-axis estimation, tri-axial magnetometer data provides a reference for yaw, reducing drift and enabling absolute heading in the Earth frame. In contrast, the 6-axis variant uses only accelerometer and gyroscope data, resulting in drift-prone yaw estimates from integrated rates. Since all flights were conducted indoors, we employed the 6-axis Madgwick filter and initialized the yaw to zero after IMU startup. Computation involves only basic vector and trigonometric operations ($O(n)$ complexity), allowing high-frequency updates suitable for the embedded platform.

Attitude estimates from the Madgwick filter serve as inputs to a PID controller for yaw stabilization. For pitch control, the measured angle is first processed by the RLS algorithm to extract the low-frequency mean before being fed to a PID controller. Gains were tuned empirically in flight to balance responsiveness and damping, accounting for inherent body-wing oscillations. The controller outputs differential commands to the CPG, which converts them into PWM signals driving the left and right wings, enabling stable maneuvers and satisfactory tracking performance. Pitch PID gains are $K_p/K_i/K_d = 0.6/0.45/0.05$ for angle offset modulation and 0.6/0.7/0.07 for stroke timing modulation. Yaw PID gains are 0.15 and 0.17 for angle offset and stroke timing modulation, respectively.

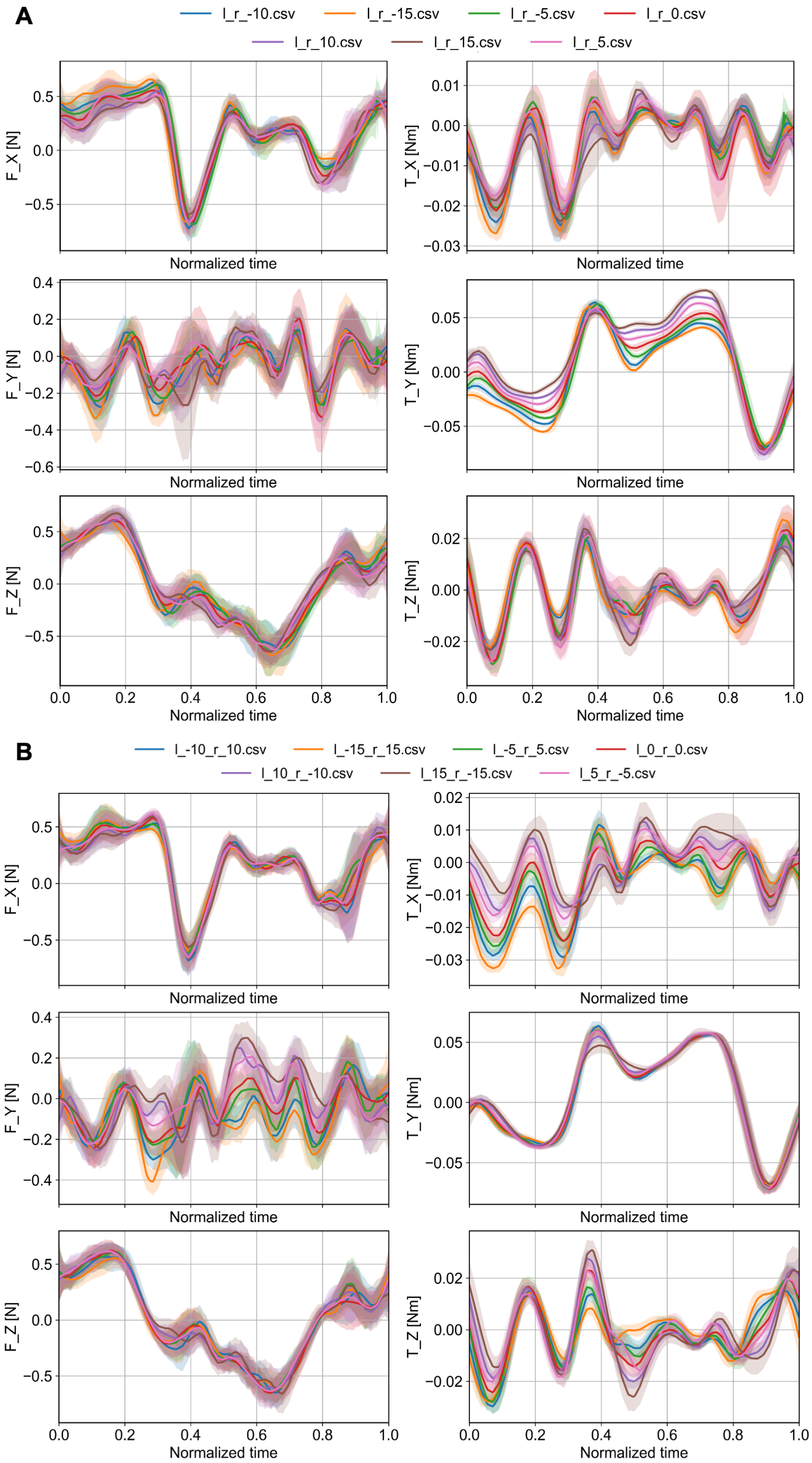

Figure S3: **Forces and torques generated by angle offset modulation.** (**A**) Symmetric modulation (`l_r_X`): both wings have an angle offset X (in deg, positive means upward). (**B**) Antisymmetric modulation (`l_X_r_Y`): left and right wings have offsets X and Y, respectively. Colors indicate different modulation settings.

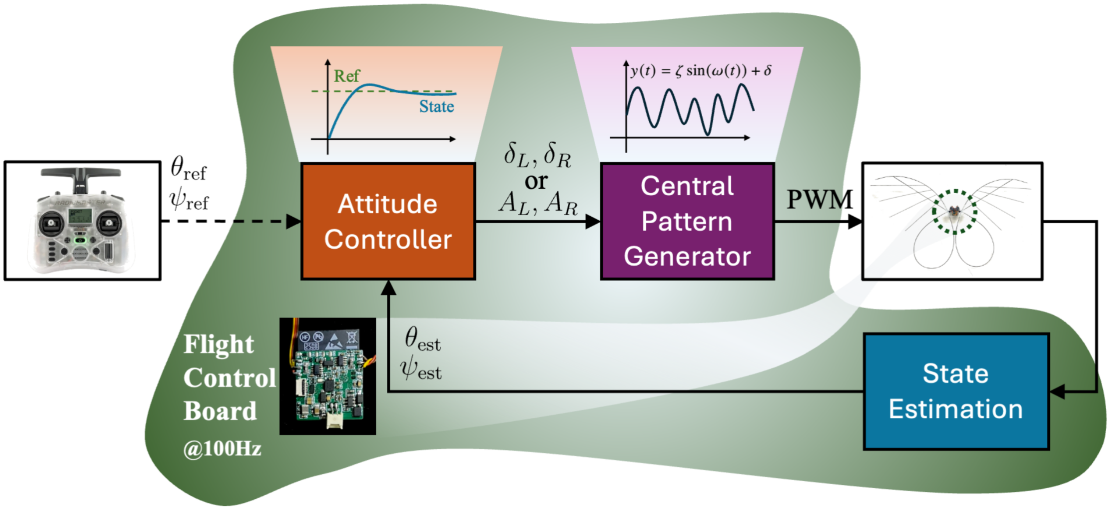

Figure S4: **Flight control architecture for attitude tracking.** Raw IMU data are fused by the onboard estimator using the Madgwick filter to provide real-time attitude feedback to the controller, which generates modulatory commands based on either wireless or preset references. CPG then converts these commands into rhythmic PWM outputs that actuate the left and right wing servos independently. All computations are executed on the flight control board at 100 Hz.

Caption for Movie S1. Overview of the AirPulse robot and demonstration of autonomous flight.

Caption for Movie S2. Fore-hind-wing phase lag and passive feathering in biomimetic wing design.

Caption for Movie S3. Characteristic body undulation in flight of a real butterfly and the AirPulse robot.

Caption for Movie S4. Demonstration of a climbing maneuver.

Caption for Movie S5. Demonstration of a turning maneuver.